

Interaction of Langmuir Turbulence and Inertial Currents in the Ocean Surface Boundary Layer under Tropical Cyclones

DONG WANG AND TOBIAS KUKULKA

University of Delaware, Newark, Delaware

BRANDON G. REICHL,^a TETSU HARA, AND ISAAC GINIS

University of Rhode Island, Narragansett, Rhode Island

PETER P. SULLIVAN

National Center for Atmospheric Research, Boulder, Colorado

(Manuscript received 15 December 2017, in final form 27 June 2018)

ABSTRACT

Based on a large-eddy simulation approach, this study investigates the response of the ocean surface boundary layer (OSBL) and Langmuir turbulence (LT) to extreme wind and complex wave forcing under tropical cyclones (TCs). The Stokes drift vector that drives LT is determined from spectral wave simulations. During maximum TC winds, LT substantially enhances the entrainment of cool water, causing rapid OSBL deepening. This coincides with relatively strong wave forcing, weak inertial currents, and shallow OSBL depth H_B , measured by smaller ratios of H_B/d_s , where d_s denotes a Stokes drift decay length scale. LT directly affects a near-surface layer whose depth H_{LT} is estimated from enhanced anisotropy ratios of velocity variances. During rapid OSBL deepening, H_{LT} is proportional to H_B , and LT efficiently transports momentum in coherent structures, locally enhancing shear instabilities in a deeper shear-driven layer, which is controlled by LT. After the TC passes, inertial currents are stronger and H_B is greater while H_{LT} is shallower and proportional to d_s . During this time, the LT-affected surface layer is too shallow to directly influence the deeper shear-driven layer, so that both layers are weakly coupled. At the same time, LT reduces surface currents that play a key role in the surface energy input at a later stage. These two factors contribute to relatively small TKE levels and entrainment rates after TC passage. Therefore, our study illustrates that inertial currents need to be taken into account for a complete understanding of LT and its effects on OSBL dynamics in TC conditions.

1. Introduction

The development of tropical cyclones (TCs) strongly depends on the air–sea interactions that include heat fluxes and momentum transfer (Emanuel 1991, 1999). The TC's strong wind and associated wave forcing drives upper-ocean currents that generate vigorous turbulence.

Turbulent eddies erode the thermocline by entraining deep cool water into the warmer upper layer, resulting in ocean surface boundary layer (OSBL) deepening and sea surface cooling (Price 1981). In turn, sea surface cooling reduces air–sea heat fluxes that drive the TC, resulting in a negative feedback between TC winds and sea surface temperature (Bender and Ginis 2000; Ginis 2002). The inertial resonance between the turning wind stress and surface currents is also a critical dynamical process under TCs because it increases the shear at the mixed layer base, leading to stronger mixing on the right-hand side of TCs (Price 1981; Skillingstad et al. 2000; Sanford et al. 2011; Sullivan et al. 2012; Reichl et al. 2016b).

Recent studies indicate that wave-driven Langmuir turbulence (LT) plays an important role in upper-ocean

^o Denotes content that is immediately available upon publication as open access.

^a Current affiliation: Program in Atmospheric and Oceanic Sciences, Princeton University, Princeton, New Jersey.

Corresponding author: Dong Wang, dongwang@udel.edu

turbulence under TCs (Sullivan et al. 2012; Rabe et al. 2015; Reichl et al. 2016b,a). LT was originally observed in moderate wind conditions as parallel bands of floating material on the sea surface, which are due to strong surface current convergences of horizontal roll vortices in the OSBL (Langmuir 1938). Over the last decades, comprehensive field observations, mostly conducted in moderate wind conditions, have revealed characteristic features of LT, such as strong surface convergence regions, downwelling jets, and the spacing of roll vortices from several meters to kilometers (Thorpe 2004; Weller and Price 1988; Farmer and Li 1995; Plueddemann et al. 1996; Smith 1992; Gargett et al. 2004; Gargett and Grosch 2014). A systematic mathematical theory of LT is based on the wave-averaged Navier–Stokes equation, the so-called Craik–Leibovich (CL) equation, and suggests that LT is driven by the CL vortex force, which is the cross-product of Stokes drift and vorticity vectors (Craik and Leibovich 1976). Physically, the Stokes drift shear tilts vertical vorticity into the direction of wave propagation, generating LT. Today LT is recognized as a fundamental upper-ocean turbulent process (McWilliams et al. 1997; Thorpe 2004; Li et al. 2005; Sullivan and McWilliams 2010; Belcher et al. 2012; D’Asaro 2014) that contributes significantly to turbulent transport and wind- and wave-driven mixed layer deepening (Kukulka et al. 2009, 2010; Grant and Belcher 2011).

Previous investigations of LT involve turbulence-resolving large-eddy simulation (LES) that is based on the filtered CL equations with explicit wave effects, which resolves LT and associated relatively large vortical structures (Skylingstad and Denbo 1995; McWilliams et al. 1997). LES studies show that LT enhances the vertical fluxes of momentum and heat, inducing stronger vertical velocity variance and mixed layer deepening (McWilliams et al. 1997; Li et al. 2005; Polton and Belcher 2007; Grant and Belcher 2009; Kukulka et al. 2009; Noh et al. 2009). Direct comparisons of LES results with ocean observations reveal that LES captures in detail many of the observed LT characteristics (Skylingstad et al. 1999; Gargett et al. 2004; Li et al. 2009; Kukulka et al. 2009, 2013; D’Asaro et al. 2014). However, most LES studies are conducted in moderate wind conditions with monochromatic waves, and only a few of them examine LT in extreme TC conditions.

Sullivan et al. (2012) explored LT dynamics under a TC by forcing an LES model with realistic TC winds and waves, which were simulated by a spectral wave model. They contrasted time series of OSBL turbulence statistics at two stations: one on the right-hand side (rhs) with strong inertial resonance and the other one on the left-hand side (lhs) with weak inertial resonance. The intensity of LT strongly depends on location and time because of

the TC’s complex wind and wave forcing, yielding more energetic LT on the rhs of the TC. Furthermore, their results indicate that the direction of roll vortices due to LT is aligned with the wind direction and tracks the Lagrangian shear direction. As a result of the TC’s transient forcing conditions, wind vector and wave propagation directions are misaligned, reducing LT intensity.

Motivated by OSBL observations of depth-averaged vertical velocity variance (VVV) obtained from Lagrangian floats under Hurricane Gustav (2008), Rabe et al. (2015) investigated OSBL turbulence with LES experiments forced by Gustav (2008)’s winds and waves. Simulated VVV is only consistent with the observed VVV with LT, that is, for simulations with CL vortex force, indicating LT’s significant role in OSBL dynamics. LES results demonstrate that LT enhances VVV and varies with complex sea states found under TCs. Misaligned wind and wave fields near the TC eye are associated with an observed suppression of VVV, which is also predicted by the LES. Thus, wind-wave misalignment can reduce VVV and suppress LT to the levels close to shear turbulence (ST).

Building on this previous work (Sullivan et al. 2012; Rabe et al. 2015), we recently designed a series of LES experiments for the full spatial TC extent to develop a turbulence closure scheme with explicit sea-state-dependent LT effects (Reichl et al. 2016b) and to investigate the role of sea-state-dependent LT in the OSBL response to TCs (Reichl et al. 2016a). In regional ocean models under TCs, which are commonly based on the Reynolds-averaged Navier–Stokes (RANS) equations, LT cannot be resolved, so that smaller-scale turbulent transport processes in the OSBL have to be parameterized. We modified the K -profile parameterization (KPP) model (Large et al. 1994) to match mean current and temperature profiles obtained from the LES model. In the KPP model, we replaced the Eulerian current with the Lagrangian current (Eulerian current plus Stokes drift) to compute the turbulent momentum flux following McWilliams et al. (2012) and also introduced turbulence enhancement factors following McWilliams and Sullivan (2000). Our new KPP model with explicit sea-state-dependent LT significantly improves estimations of LES temperature and currents compared to results of the standard (unmodified) KPP model (Reichl et al. 2016b). We next introduced this new KPP model in a regional three-dimensional coupled wave–ocean RANS model to demonstrate that sea-state-dependent LT substantially modifies the three-dimensional OSBL response (Reichl et al. 2016a). Results indicate that LT reduces upwelling and horizontal advection as a result of enhanced near-surface mixing and that simulations without sea-state-dependent LT cannot accurately reproduce the sea surface cooling and

horizontal transport. More recently, Blair et al. (2017) investigated the upper-ocean response under Hurricane Edouard (2014) with our new KPP model and satellite observations, suggesting the importance of sea-state-dependent LT on the mixed layer depth evolution.

In this study, we use the same LES approach as in Reichl et al. (2016b) to comprehensively investigate LT dynamics, OSBL energetics, and the influence of inertial currents on the OSBL evolution for a wide range of realistic TC conditions. We first review our basic numerical approach and provide an overview of complex wind and wave conditions under TCs (section 2) and then illustrate that the LT-driven OSBL is not only sea-state dependent but also influenced by inertial currents in TC conditions (section 3).

2. OSBL turbulence model

To analyze LT in TC conditions, we use the same wind, wave, and turbulence modeling approaches and datasets as in our previous study (Reichl et al. 2016b), which are briefly reviewed in the following subsections.

$$C_d = \begin{cases} 0.0012, & U_{10} < 11 \text{ m s}^{-1}, \\ (0.49 + 0.065U_{10}) \times 10^{-3}, & 11 \text{ m s}^{-1} < U_{10} < 25 \text{ m s}^{-1}, \\ 1.8 \times 10^{-3}, & 25 \text{ m s}^{-1} < U_{10}. \end{cases} \quad (1)$$

Recent studies show the complexity of drag coefficient under TCs, which varies with different storm quadrants and even wind directions (Holthuijzen et al. 2012; Hsu et al. 2017). Since there is substantial uncertainty of the drag coefficient, we adopt Eq. (1) with simpler assumptions than what has been done in previous studies (Sullivan et al. 2012; Rabe et al. 2015; Reichl et al. 2016b).

b. LES model and numerical experiments setups

Following previous approaches (McWilliams et al. 1997; Skillingstad and Denbo 1995; Kukulka et al. 2010), we use an LES model to simulate the upper-ocean response to TC's wind and wave fields. The LES model solves the grid-filtered CL equations (Craig and Leibovich 1976). LT is generated by the Craik–Leibovich vortex force, which is the cross-product of the Stokes drift \mathbf{u}_s and vorticity. When the wave effect is not considered ($\mathbf{u}_s = 0$), the LES model simply solves grid-filtered Navier–Stokes equations that only generate ST. The Stokes drift is obtained through the wave model, introduced in the following section (section 2c). We only solve the density equation in the LES model and assume that temperature is linearly related to density by

a. Wind model

The TC wind field is constructed based on a Holland wind model (Holland 1980, 2008) with the radius of maximum wind (RMW) of 50 km, maximum wind speed at 10-m height of 65 m s^{-1} , and a translation speed of 5 m s^{-1} , which represent typical TC parameters (Reichl et al. 2016b). The output of the wind model is the wind velocity at 10-m height with speed U_{10} over a domain with a length from -648 to 648 km in the TC's propagation direction (along X) and a width from -500 to 500 km across the TC's propagation direction (along Y) (Fig. 1, top left). In addition to the horizontally averaged turbulent statistics investigated by Reichl et al. (2016b), in this study we also output and investigate the four-dimensional spatiotemporal high-resolution LES temperature, pressure, and velocity fields.

The wind stress vector at the sea surface has the same direction as the wind velocity, and its magnitude is parameterized by $\tau = \rho_a C_d U_{10}^2$, where ρ_a is the air density and C_d is the drag coefficient that depends on U_{10} as follows (Sullivan et al. 2012):

$$\gamma = -\frac{1}{\rho_0} \frac{\partial \rho}{\partial T}, \quad (2)$$

where ρ is the water density, $\rho_0 = 1024 \text{ kg m}^{-3}$ is the reference density, T is water temperature, and $\gamma = 2 \times 10^{-4} \text{ K}^{-1}$ is the thermal expansion coefficient.

LES experiments are performed for 18 stations across the TC translation direction along Y from -200 to 200 km, with a minimum and maximum spacing between stations of 20 and 50 km, respectively (Table 1). The coordinate Y is zero at the TC center, and $Y > 0$ and $Y < 0$ are on the rhs and lhs of the TC eye, respectively. The LES domain size spans horizontally $750 \text{ m} \times 750 \text{ m}$ and is 240 m deep with 256 grid points in each direction for experiments in Table 1. Inside the LES domain we use x_i with index $i = 1, 2, 3$ to denote the spatial coordinate (x, y, z) in east, north, and vertical directions, respectively. For all experiments the initial potential temperature profile features a 10-m homogeneous mixed layer with $T = 302.4 \text{ K}$ and a constant stratification with $dT/dz = 0.04 \text{ K m}^{-1}$ below the mixed layer, where z denotes the depth. Small constant surface cooling of -5 W m^{-2} is imposed (McWilliams et al. 1997) for all simulations, which facilitates the initial

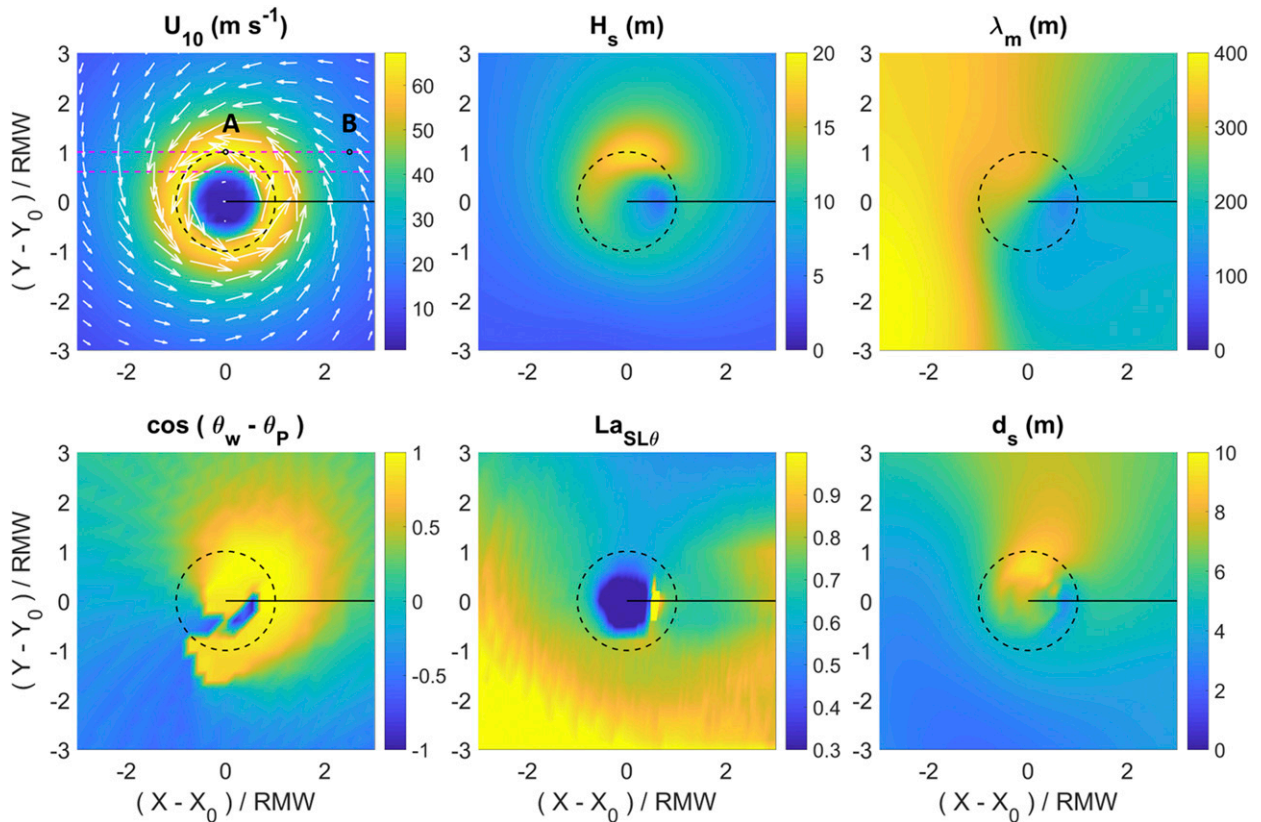


FIG. 1. TC's (top left) wind direction and magnitude U_{10} , (top center) significant wave height H_s , (top right) mean wavelength λ_m , (bottom left) the wind and peak wave spectrum misalignments, (bottom center) the projected surface layer Langmuir number $La_{SL\theta}$, and (bottom right) the depth scale of Stokes drift shear d_s . The black dashed line denotes the RMW, and the black solid line indicates the path of the TC moving from right to left. The dashed magenta lines denote two LES transects which will be examined in the main text. The two black circles on one transect, marked by capital letters A and B, are two locations that will be discussed in detail. Note that the x axis represents the translating distance of the TC, and the y axis indicates the distance of each station from the TC's path. Both distances are normalized by the RMW. The TC travels from right to left, and $(X - X_0) = 0$ is where the TC's eye passes.

spinup of turbulence but is otherwise insignificant for the OSBL dynamics presented here. The LES model is forced at the surface with the modeled wind stress vector (section 2a), and the Stokes drift vector \mathbf{u}_s is imposed based on simulated 2D wave height spectra (section 2c).

c. Wave simulation

1) WAVE MODEL

The third-generation wave model WAVEWATCH III (Tolman 2009) is used to simulate the directional

frequency spectra of surface gravity waves in TC conditions following Reichl et al. (2016b). Its computational domain is 3000 km long in the TC's translation direction and 1800 km wide across the TC's translation direction. The wave model has a horizontal grid spacing of 8.33 km, and the wave spectrum is discretized into 48 evenly spaced directions and 40 logarithmically spaced frequencies. The simulated wave field is stationary in a coordinate system translating with the TC. The skill of WAVEWATCH III physics parameterizations to simulate complex features of the wave field on the left of the translation direction remains a topic of research (see

TABLE 1. Locations of 18 stations in LES experiments.

Station No.	1	2	3	4	5	6	7	8	9
$Y - Y_0$ (km)	200	150	130	110	90	70	50	30	10
Station No.	10	11	12	13	14	15	16	17	18
$Y - Y_0$ (km)	0	-20	-40	-60	-80	-100	-120	-140	-200

Hsu et al. 2018). However, comparison of the version of WAVEWATCH III employed for this study with wave observations shows good skill on average to predict the sea state under extreme hurricane conditions (Fan et al. 2009).

The most energetic wave fields with large H_s and long λ_m are found on the rhs of the TC near the RMW at $(Y - Y_0)/\text{RMW} = 1$ (Fig. 1, top center and top right). This is because waves travel with the TC and are thus exposed to greater wind forcing, creating favorable conditions for wave development. Note that the TC translates from right [$(X - X_0) > 0$] to left [$(X - X_0) < 0$], and the X axis is equivalent to time $t = (X - X_0)/(5 \text{ m s}^{-1})$. In contrast, waves on the lhs are much weaker with smaller λ_m and H_s because the wind direction opposes the TC direction. Longer waves far ahead of the TC near $(X - X_0)/\text{RMW} = -2$ indicate the presence of fast-traveling swell waves, but their H_s value is small so these waves do not significantly contribute to wave forcing (Fig. 1, top right). As waves are more developed on the rhs of the TC, the misalignment between the wind direction θ_w and the peak wave spectrum θ_p is smaller on the rhs (Fig. 1, bottom left). In other regions under the TC, however, the propagation direction of energetic waves differs significantly from the wind direction, in particular on the lhs.

2) WAVE PARAMETERS CONTROLLING LT

The time- and space-dependent Stokes drift in the LES model is obtained by integrating the simulated wave spectra (Kenyon 1969):

$$\mathbf{u}_s(z) = 2 \int_0^\infty \int_{-\pi}^\pi \mathbf{k} \omega F(\omega, \theta) e^{2kz} d\theta d\omega, \quad (3)$$

where $F(\omega, \theta)$ is the two-dimensional wave height spectrum, \mathbf{k} is the horizontal wavenumber vector, $k = |\mathbf{k}|$ denotes its magnitude, ω is the radian frequency, and θ is the wave propagation direction. It is assumed that surface gravity waves satisfy the deep-water dispersion relation $\omega = \sqrt{gk}$, where g is the acceleration of gravity. Note that the largest parameterized wavenumber in the model is 400 m^{-1} , which specifies the upper bound of radian frequency in Eq. (3) (Reichl et al. 2016b).

Strong wind-wave misalignment in TC conditions reduces LT's intensity (Sullivan et al. 2012; Rabe et al. 2015; Reichl et al. 2016b). To scale LT for conditions with wind-wave misalignment, Van Roekel et al. (2012) modified the surface layer Langmuir number from Harcourt and D'Asaro (2008) that scales LT forced by equilibrium wind-wave spectra. The so-called projected surface layer Langmuir number projects the wind and wave forcing onto the Langmuir cell direction and is given by

$$\text{La}_{\text{SL}\theta} = \sqrt{\frac{u_* \cos(\theta_w - \alpha)}{\left| \frac{\cos(\theta_s - \alpha)}{0.2H_B} \int_{-0.2H_B}^0 \mathbf{u}_s dz \right|}}, \quad (4)$$

where θ_w is the wind direction, θ_s is the direction of depth-averaged Stokes drift within $0.2H_B$, and α is the direction of the depth-averaged Lagrangian shear, which is an estimate for the direction of Langmuir cells and defined by

$$\tan(\alpha) = \frac{\int_{-0.2H_B}^0 \frac{\partial(\langle v \rangle + v_s)}{\partial z} dz}{\int_{-0.2H_B}^0 \frac{\partial(\langle u \rangle + u_s)}{\partial z} dz}. \quad (5)$$

The Eulerian current and the Stokes drift in the (x, y) direction are denoted as (u, v) and (u_s, v_s) , respectively, and $\langle \rangle$ denotes a horizontal spatial average inside the LES numerical domain. The spatial distribution of $\text{La}_{\text{SL}\theta}$ with relatively small $\text{La}_{\text{SL}\theta}$ values (Fig. 1, bottom center) indicates that LT plays an important role in OSBL dynamics and that LT is stronger on the rhs (Reichl et al. 2016b). Interestingly, small values of $\text{La}_{\text{SL}\theta}$ do not always coincide with large values of H_s and λ_m , suggesting that LT is not necessarily more pronounced for more energetic or more developed wave fields.

Recent studies show that the Stokes drift decay length scale influences the dynamics and structure of LT (Sullivan et al. 2012; Gargett and Grosch 2014; Kukulka and Harcourt 2017). To account for the effects of Stokes drift shear for wave spectra, we compute the length scale d_s for the depth-averaged Stokes drift shear as

$$d_s = \frac{\left| \int_{-\infty}^0 \mathbf{u}_s(z) dz \right|}{|\mathbf{u}_s(0) - \mathbf{u}_s(-\infty)|}. \quad (6)$$

In TC conditions, we find that d_s is closely related to the penetration depth scale of the Stokes drift introduced by Sullivan et al. (2012), for which the misalignment between surface Stokes drift and Stokes drift at greater depth is considered. The differences between d_s and λ_m in TC conditions further illustrate that λ_m is a poor estimator of Stokes drift decay length scale that drives LT (Fig. 1, top right and bottom right). In summary, traditional parameters that describe the sea state are not sufficient to characterize LT dynamics in TC conditions.

3. Results

We first investigate the response of the OSBL to tropical cyclones and identify regions of relatively large

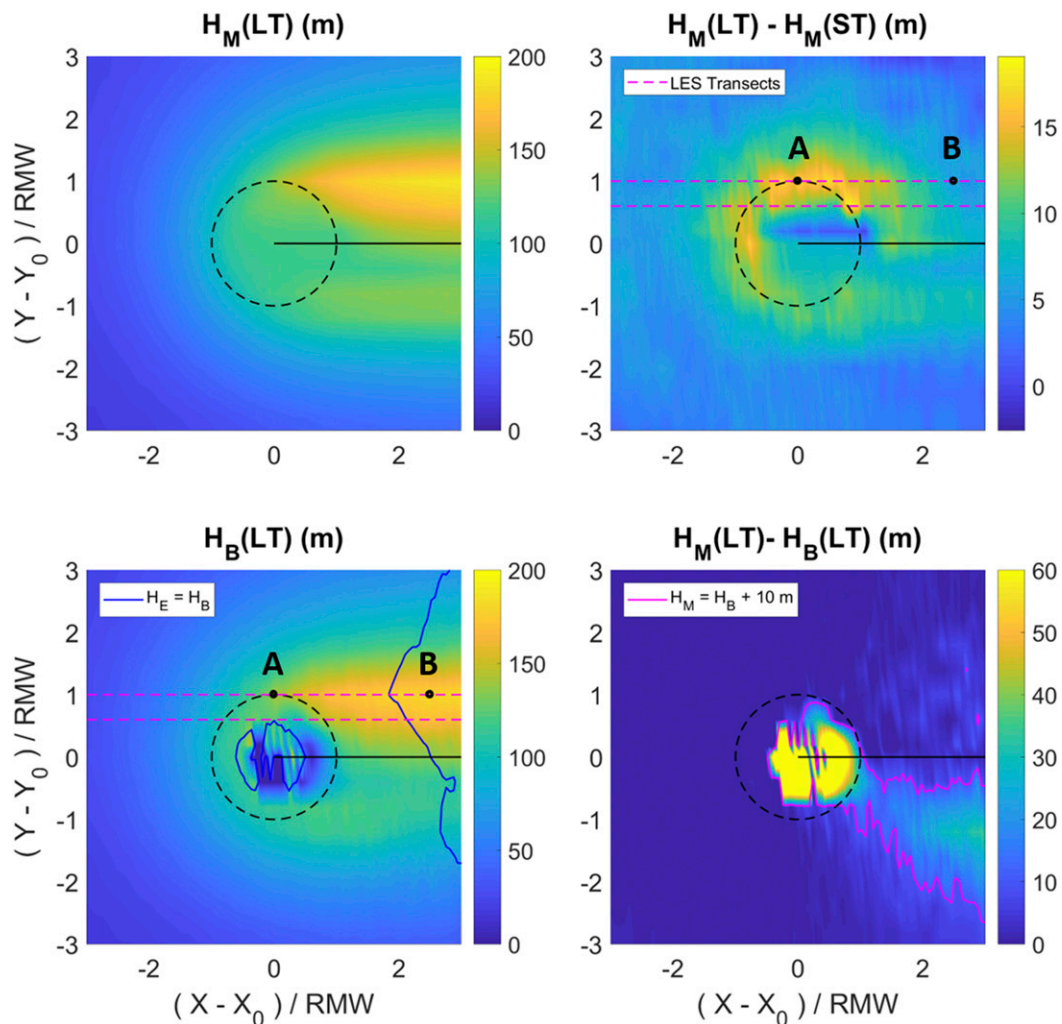


FIG. 2. (top left) The mixed layer depth H_M for the LT case, (top right) the difference of H_M between the LT case and the ST case, (bottom left) turbulent boundary layer depth H_B , and (bottom right) the difference between H_M and H_B for the LT case. The regions enclosed by the solid blue contours with $(X - X_0)/RMW > 2$ are where H_E is shallower than H_B in the bottom left panel. The lhs regions enclosed by the solid magenta contours with $(X - X_0)/RMW > 0$ are where the mixed layer depth is more than 10 m deeper than the boundary layer depth in the bottom right. Other line styles have the same meaning as in Fig. 1.

entrainment of deep cold water into the OSBL for the LT and ST cases (section 3a). Then we investigate different mechanisms that induce greater entrainment in the LT case (section 3b) and the ST case (section 3c).

a. The response of OSBL to tropical cyclones

1) OSBL DEPTH

The cold wake under the TC is caused by upper-ocean mixing accompanied by mixed layer deepening (Price 1981; Sullivan et al. 2012). The mixed layer depth H_M is defined as the depth of largest temperature gradient where the stratification is strongest. The spatial and

temporal distribution of H_M shows an unsymmetrical pattern with greater H_M on the rhs of the TC due to resonant wind forcing that drives strong inertial currents (Price 1981; Skillingstad et al. 2000; Sanford et al. 2011) (Fig. 2, top left). LT enhances mixed layer deepening, and the contribution of LT is spatially variant (Fig. 2, top right). Enhanced mixed layer deepening due to LT is most pronounced near the RMW, especially on the rhs of the TC where strong, wind-aligned waves create favorable conditions for LT (cf. the forcing shown in the Fig. 1). However, after the storm passes, H_M in both LT and ST cases approaches a similar final value on the rhs of the TC (Fig. 2, top right). This suggests greater

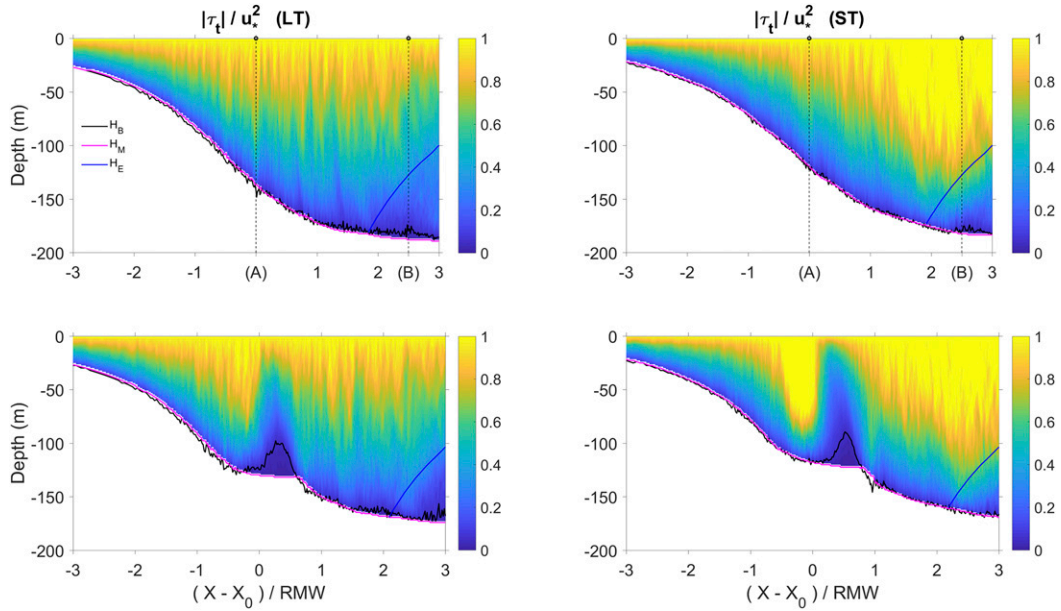


FIG. 3. LES transect of normalized turbulent stress profiles at (top) $(Y - Y_0)/RMW = 1$ and (bottom) $(Y - Y_0)/RMW = 0.6$ for (left) the LT cases and (right) the ST cases. Locations A and B are denoted by the black dashed lines. The solid magenta line denotes the mixed layer depth H_M , and the solid black line indicates the boundary layer depth H_B . The turbulent Ekman layer depth is denoted by the solid blue line, and note that we do not show H_E that is below H_M .

entrainment of cool water into the OSBL for the ST case when the wind subsides, which compensates the smaller mixed layer deepening near the RMW, finally resulting in a similar H_M .

Because of the highly transient forcing conditions under TCs, it is useful to introduce an OSBL depth characterized by active turbulent mixing. Following previous approaches for atmospheric boundary layer turbulence (Zilitinkevich et al. 2007), we specify a turbulent boundary layer depth H_B where the turbulent stress decays to 5% of its surface value. Figure 3 shows the normalized turbulent stress profiles at two example transects with two specific locations (transects are denoted by a dashed magenta line and locations are marked with A and B in the bottom left of Fig. 2). Location A is on the rhs of the TC near the RMW where LT rapidly changes H_M . Location B is also on the rhs but about 2.5 times the RMW behind the TC’s eye in a region where H_M is similar for the LT and ST case.

As expected, H_B is close to H_M during rapid mixed layer deepening and strong wind and wave forcing (regions outside the solid magenta contour in the bottom right of Fig. 2). However, under the eye, where winds and turbulence levels are relatively weak, H_M does not accurately characterize the boundary layer depth because H_B is much smaller than H_M (regions with positive values in the bottom right of Fig. 2). Across the TC eye,

the winds decrease for $-1 < (X - X_0)/RMW < 0$, and the normalized turbulent stress is relatively large owing to relatively strong residual turbulence (Fig. 3, bottom). After the eye passes for $0 < (X - X_0)/RMW < 1$, the normalized turbulent stress is relatively small as a result of relatively weak residual turbulence. These history effects are more pronounced for the ST case, which indicates that the turbulence in the LT case is more responsive to the transient TC forcing.

Behind the TC eye, we observe active turbulence ($|\tau_t|/u_*^2 > 0.2$) at great depth ($z < -0.5H_B$), although winds are weak (Fig. 3, top). The turbulent stress profile in the ST case shows a more homogenized structure in the upper OSBL ($z > -0.5H_B$) (Fig. 3, top right), while the turbulent stress in the LT case decays faster with depth after the TC passes (Fig. 3, top left). This difference in stress profiles is related to more energetic inertial currents in the ST case (discussed in section 3c).

To further examine the effect of TC’s transient forcing on the OSBL depth over the extent of the whole TC domain, we compare H_B to an estimate of Ekman layer depth: $H_E = 0.25u_*/f$, following McWilliams et al. (1997) (Fig. 2, bottom left). For typical wind-driven Ekman layers, current shear is small below H_E , and, thus, turbulence levels are negligible. However, our results reveal regions for which H_B exceeds H_E , illustrating increased turbulence levels below H_E [regions mostly on

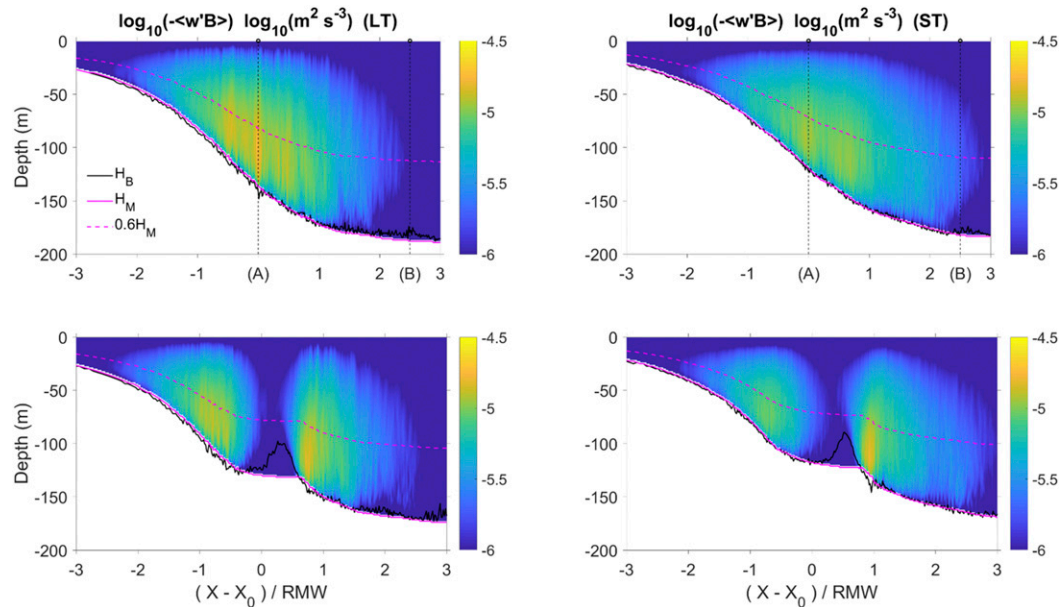


FIG. 4. LES transect of buoyancy fluxes at (top) $(Y - Y_0)/RMW = 1$ and (bottom) $(Y - Y_0)/RMW = 0.6$ for (left) the LT cases and (right) the ST cases. Note that the buoyancy fluxes in the plot are in the logarithmic form with a base of 10. The dashed magenta line indicates $0.6H_M$, and other line styles are as in Fig. 3.

the rhs with $(X - X_0)/RMW > 2$ enclosed by the solid blue contour in the bottom left of Fig. 2]. For $(X - X_0)/RMW > 1.8$, H_B exceeds H_E , suggesting the generation of turbulence that is due to inertial currents instead of local winds (Fig. 3). Such relatively large $H_B > H_E$ and the persistent mixed layer deepening behind the TC eye suggest the importance of inertial currents in influencing OSBL dynamics.

2) ENTRAINMENT

To understand how turbulence drives OSBL deepening, we first examine the evolution of profiles of the resolved turbulent buoyancy fluxes $-\langle w'B \rangle$ at two transects (Fig. 4). Here $B = \rho'g/\rho_0$ is the buoyancy, w is the vertical velocity, and the prime denotes the deviation from the horizontal average denoted by symbol $\langle \rangle$.

For both the LT and ST cases, the greatest buoyant fluxes occur below $0.6H_M$, which is in the region of the shear layer. The shear layer is defined as the layer with pronounced stratification and mean current shear and approximately locates below $0.6H_M$ (temperature and current profiles will be shown in sections 3b and 3c) (Skylingstad et al. 2000; Grant and Belcher 2011).

For the transect that is tangential to the RMW, the buoyancy fluxes in the LT case are larger than in the ST case near the maximum wind period (location A), suggesting that LT enhances buoyancy fluxes that contribute to enhanced mixed layer deepening (Fig. 4, top left).

However, buoyancy fluxes in the ST case increase behind the TC eye and are about one order larger than in the LT case at $(X - X_0)/RMW = 2.5$ (location B) (Fig. 4, top right). This is consistent with the relatively strong mixed layer deepening in the ST case behind the TC eye, which is due to the turbulence induced by strong inertial currents.

For the transect crossing the TC's eye region, we observe two periods with strong buoyancy fluxes for both the LT and ST case, which corresponds to the timing of two maximum winds as the TC eye passes (Fig. 4, bottom). The peaks of the buoyancy fluxes in the LT case are greater than in the ST case, indicating LT's significant role in enhancing the turbulent mixing even under transient winds. Greater buoyancy fluxes in the ST case are not found until $(X - X_0)/RMW > 2$, where H_B is deeper than H_E , suggesting the presence of shear-driven turbulence due to energetic inertial currents (Fig. 2, bottom left).

To identify the influence of LT and inertial currents on mixed layer deepening over the full spatial extent of the TC, we examine the depth-integrated buoyancy fluxes, which drive changes in total (depth integrated) potential energy as

$$\frac{d}{dt} \int_{-H}^0 zg \frac{\langle \rho \rangle}{\rho_0} dz = \int_{-H}^0 -\langle w'B \rangle dz + \text{SGS}, \quad (7)$$

where SGS symbolizes subgridscale density fluxes (second term on the rhs), and H is the depth of LES domain.

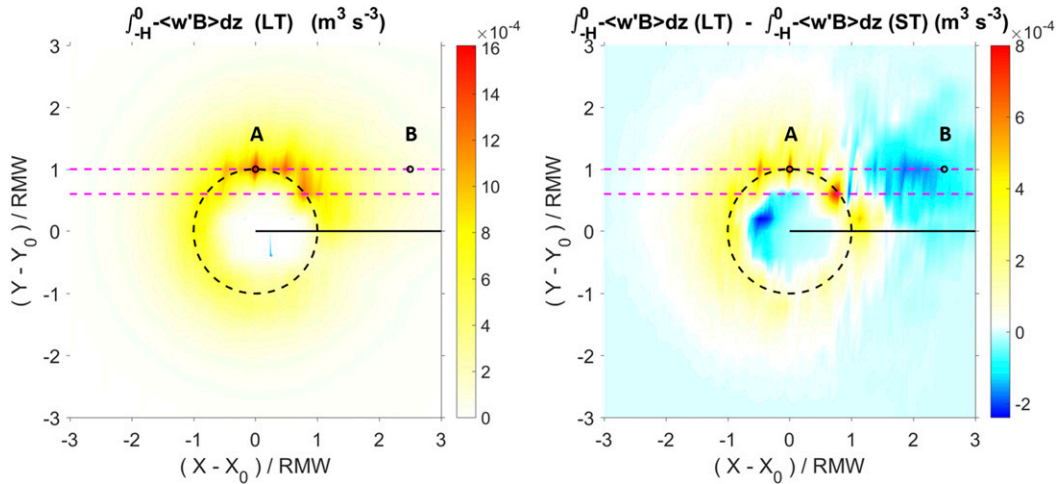


FIG. 5. (left) The depth-integrated buoyancy fluxes $\int_{-H}^0 -\langle w'B \rangle dz$ within the computation depth in the LT case and (right) the difference of $\int_{-H}^0 -\langle w'B \rangle dz$ between the LT case and the ST case. The line styles have the same meaning as in Fig. 1.

The greatest depth-integrated buoyancy flux occurs around the maximum wind radius where the maximum mixed layer deepening rates are also found (Fig. 5, left). The stronger turbulent buoyancy transport on the rhs agrees with the larger mixed layer deepening on the rhs (Fig. 2, top left). Pronounced differences of $\int_{-H}^0 -\langle w'B \rangle dz$ between the LT and the ST cases show that the enhanced entrainment by LT mainly occurs near the RMW (Fig. 5, right). In the ST case, entrainment is greater inside the TC eye as the result of enhanced leftover turbulence under transient winds (Fig. 3, bottom right). The greater entrainment on the rhs behind the TC eye is caused by the stronger turbulence generated by inertial currents (section 3c).

To explore the relation of wind forcing to entrainment, we scale the depth-integrated buoyancy fluxes $\int_{-H}^0 -\langle w'B \rangle dz$ by u_*^3 , which is similar to the scaling proposed by Grant and Belcher (2009) (Fig. 6). In both the LT and the ST cases, significant deviations from this scaling are observed. Smaller values of $\int_{-H}^0 -\langle w'B \rangle dz$ are mainly found on the lhs of the storm, while greater values of $\int_{-H}^0 -\langle w'B \rangle dz$ are located mostly on its rhs (Fig. 6, left and center). In the ST case differences are caused by energetic inertial currents on the rhs, inducing shear-driven turbulent mixing. This is consistent with the stronger buoyancy fluxes and more homogenized turbulence stress profiles on the rhs, behind the TC eye.

In the LT case, differences are due to LT that is more vigorous on the rhs due to stronger wave forcing and weaker on the lhs due to wind-wave misalignment (refer to Fig. 1). To examine the influence of LT on entrainment under the TC's complicated wind and wave forcing, we consider a similar scaling approach as Grant and Belcher (2009) but replace La_t with $La_{SL\theta}$, which is more

adequate in complex wind and wave conditions, so that $\int_{-H}^0 -\langle w'B \rangle dz$ is expected to scale with $La_{SL\theta}^{-2} u_*^3$. This scaling significantly reduces the scatter, illustrating the importance of sea-state-dependent Langmuir turbulence in buoyancy entrainment (Fig. 6, right).

b. Enhanced entrainment due to LT

For aligned wind-wave conditions and relatively shallow mixed layers, LT enhances turbulent entrainment through a three-step process: first the large coherent structures in LT facilitate the transport of momentum through the boundary layer; then the shear-instability near the mixed layer base is locally enhanced, inducing greater erosion of thermocline; finally, the eroded colder water is transported upward and mixed by LT near the surface (Kukulka et al. 2010). In this section, we evaluate this process step by step in tropical cyclone conditions by examining the flow field at a location where enhanced mixed layer deepening and greater buoyancy fluxes due to LT are found (marked with A in the bottom of Fig. 2).

1) CURRENT AND TEMPERATURE PROFILES

To address the enhanced shear instability by LT, we first examine the horizontally averaged Lagrangian current and temperature profiles at a location A (Fig. 7, top). The Lagrangian current is the sum of the Eulerian current and Stokes drift. To better illustrate the relation between wind and current directions, we project the horizontal Eulerian currents and Stokes drift into the along-wind and crosswind direction denoted by subscripts // and \perp , respectively (Fig. 7, top left).

At location A, both the LT and the ST cases show predominant along-wind Eulerian currents compared to the

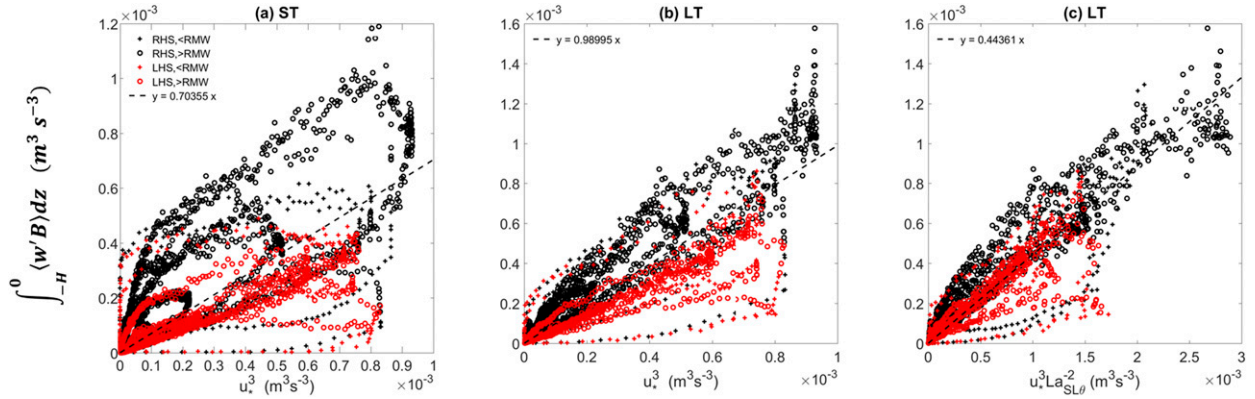


FIG. 6. The scaling of depth-integrated buoyancy fluxes $\int_{-H}^0 \langle w'B \rangle dz$ by u_*^3 for both (left) the ST case and (center) the LT case. (right) The scaling of $\int_{-H}^0 \langle w'B \rangle dz$ by $La_{SL\theta}^{-2} u_*^3$ for the LT case. Crosses denote locations inside the RMW, and circles denote locations outside the RMW. Black colors indicate locations on the rhs of the TC, and red colors indicate locations on the lhs of the TC. The black dashed line is the linear regression of the scatter.

crosswind currents. This is because the onset of the TC's maximum wind mainly accelerates currents and the inertial currents have not fully spun up yet. With LT, the vertical profile of $\langle u \rangle_{||}$ is more uniform in the upper OSBL with $z > -0.5H_B$ compared to the ST case (Fig. 7, top left). Large coherent structures in the presence of LT efficiently transport momentum downward, which homogenizes the upper OSBL and decreases the shear in the mean Eulerian currents. However, the near-surface Lagrangian current shear is more alike in both cases, illustrating the predominant Stokes drift shear in the LT case. In addition, the currents in the LT and the ST cases are also similar in the shear layer ($z < -0.6H_B$), although the buoyancy entrainment at the mixed layer base substantially differs in both cases.

To assess the influence of stratification on entrainment, we also investigate the temperature profiles at location A. The OSBL temperature with LT is about 0.5K lower than without LT because of the enhanced entrainment (Fig. 7, top center). Within the shear layer, the temperature gradient in the LT case is slightly greater than the ST case, implying stronger stratification. To better understand the competition between destabilizing current shear and stabilizing stratification, we examine the gradient Richardson number:

$$Ri = \frac{-\frac{g}{\rho_0} \frac{d\langle \rho \rangle}{dz}}{\left(\frac{d\langle u \rangle}{dz} \right)^2 + \left(\frac{d\langle v \rangle}{dz} \right)^2}. \quad (8)$$

In the ST case, Ri gradually increases with depth and approaches a value close to the critical value ($Ri = 0.25$) near the mixed layer base (solid red line in the top right of Fig. 7). In the LT case, Ri significantly exceeds 0.25 in the upper half of the OSBL because currents

are homogenized, illustrating the importance of LT in generating turbulence (solid black line in the top right of Fig. 7). In the lower half of the OSBL, Ri approaches a local minimum near H_B , indicating the importance of locally generated shear instability that effectively erodes the thermocline and enhances entrainment of cool water (Kukulka et al. 2010).

2) VELOCITY VARIANCE AND TURBULENT ANISOTROPY

To further address the locally enhanced shear instability by LT, we examine the velocity variance profile whose anisotropy and magnitude characterize the turbulence's type and intensity, respectively.

At location A with LT, the normalized $\langle w'^2 \rangle$ has a peak value that is larger than both $\langle u'^2 \rangle$ and $\langle v'^2 \rangle$ at the depth of $0.2H_B$, which is induced by strong downwelling flows due to LT (Fig. 8, top left). Relatively large $\langle v'^2 \rangle$ near the surface ($z > -0.4H_B$) is associated with strong LT crosswind convergence regions above downwelling flows (note that x is approximately aligned with the wind) (Thorpe 2004). Below $0.4H_B$, horizontal velocity variances are larger than $\langle w'^2 \rangle$, suggesting that shear-driven turbulence is dominant at greater depth ($z < -0.4H_B$). Enhanced $\langle u'^2 \rangle$ near the bottom of the OSBL indicates enhanced shear-driven turbulence at the OSBL base due to a greater momentum transport, which is expected for rapid mixed layer deepening with LT (Kukulka et al. 2010). In the ST case, normalized $\langle w'^2 \rangle$ in the upper half of the OSBL is much smaller than in the LT case and $\langle u'^2 \rangle$ is always larger than $\langle v'^2 \rangle$ throughout the OSBL as expected for shear-driven turbulence (Fig. 8, top right). In addition, the peak in horizontal velocity variances near the OSBL base is absent.

The profiles of velocity variances in Fig. 8 demonstrate that LT changes the anisotropy of velocity

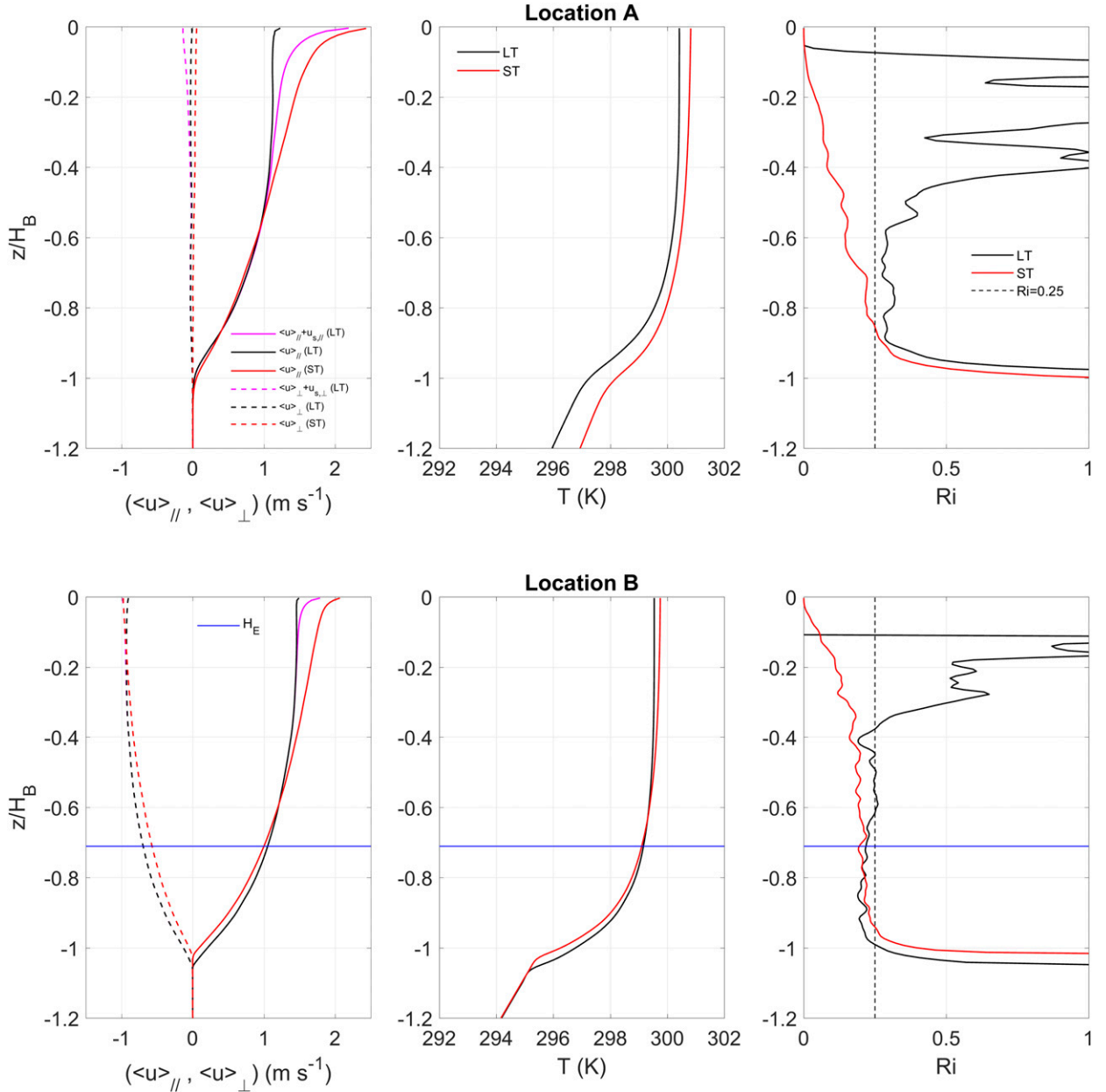


FIG. 7. The profiles of (left) along-wind (solid lines) and crosswind currents (dashed lines), (center) temperature, and (right) gradient Richardson number at (top) location A and (bottom) location B with LT (black lines) and without LT (ST) (red lines). The solid and dashed magenta lines in the left panels denote Lagrangian currents in the along-wind and crosswind direction, respectively. The thin black dashed lines in the right panels denote $Ri = 0.25$, and the solid blue lines in the bottom panels indicate the Ekman layer depth H_E .

variances, inducing a larger vertical velocity variance in the upper OSBL ($z > -0.4H_B$). Therefore, the anisotropy of velocity variances is used as a metric to distinguish the regime dominated by LT or ST in the upper part of the OSBL. Here we introduce a turbulent anisotropy ratio R_t as the ratio of vertical to horizontal velocity variances following (e.g., Polton and Belcher 2007; Rabe et al. 2015)

$$R_t = \frac{\langle w^2 \rangle}{\langle u^2 \rangle + \langle v^2 \rangle}. \quad (9)$$

In the ST case, R_t is smaller (< 0.3) without much depth variation (Fig. 9, bottom). With LT, we define the depth H_{LT} with $R_t > 0.5$ down to which LT is dominant (Fig. 9, top). Our results indicate that $H_{LT} \approx 0.4H_B$ for

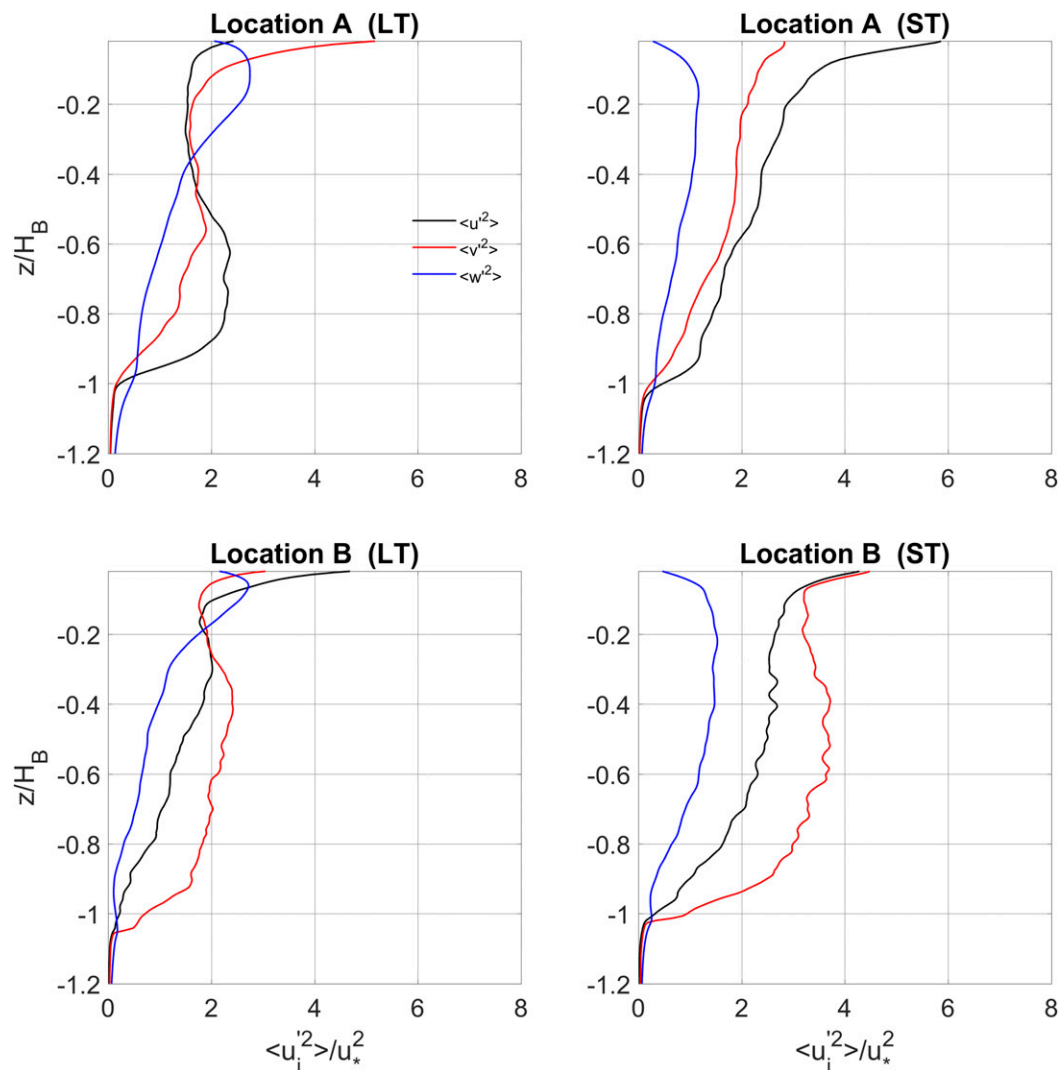


FIG. 8. The profiles of normalized velocity variances by u_*^2 at (top) location A and (bottom) location B (left) with LT and (right) without LT (ST): $\langle u'^2 \rangle$ (solid black), $\langle v'^2 \rangle$ (solid red), $\langle w'^2 \rangle$ (solid blue).

sufficiently large d_s/H_B (black dashed line in the top panel of Fig. 9). For smaller d_s/H_B , the Stokes drift decay length controls H_{LT} (Kukulka and Harcourt 2017), and we find $H_{LT} \approx 6.5d_s$ (magenta dashed line in the top panel of Fig. 9). We find that rapid mixed layer deepening due to LT only occurs for $0.4H_B < 6.5d_s$, which is consistent with Sullivan et al. (2012). In our simulations, this criterion is met before the TC passes, suggesting that LT-enhanced entrainment mainly occurs before the TC passes.

3) TKE BUDGET

To investigate enhanced turbulent kinetic energy (TKE) production and different mechanisms, we examine the budget of resolved TKE:

$$\begin{aligned} \frac{\partial \langle u'_i u'_i \rangle / 2}{\partial t} = & -\langle w' u'_i \rangle \frac{\partial \langle u'_i \rangle}{\partial z} - \langle w' u'_i \rangle \frac{\partial u_{s,i}}{\partial z} - \frac{g}{\rho_0} \langle w' \rho' \rangle \\ & - \frac{\partial}{\partial z} \left(\frac{1}{2} \langle u'_i u'_i w' \rangle + \frac{1}{\rho_0} \langle w' p' \rangle \right) + \langle \varepsilon \rangle + \text{SGS}. \end{aligned} \quad (10)$$

The Eulerian shear production P_E [first term on the rhs of Eq. (10)] and the Stokes drift shear production P_S [second term on the rhs of Eq. (10)] are two source terms that generate most of the TKE. The remaining terms in Eq. (10) from left to right are buoyancy flux (third term), divergence of the energy fluxes due to TKE advection (fourth term), rate of turbulent pressure work (fifth term), and TKE dissipation rate due to subgrid-scale motion (sixth term). The SGS is the sum of all remaining

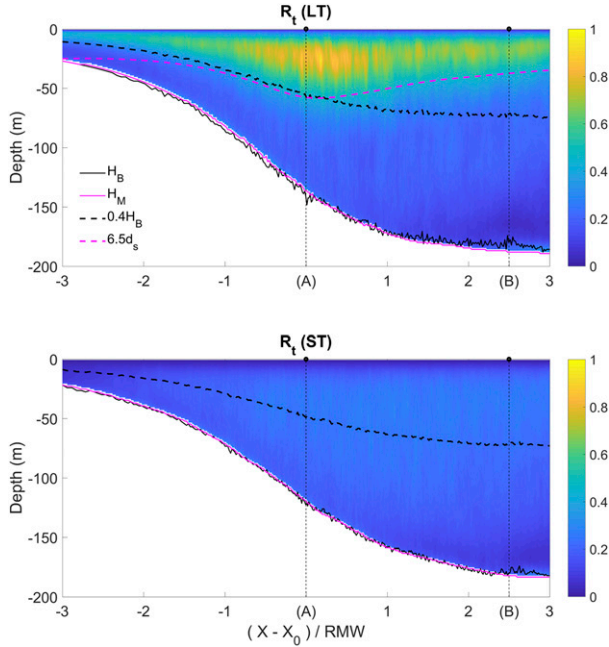


FIG. 9. LES transect of turbulent anisotropy R_t for (top) the LT case and (bottom) the ST case. The dashed magenta line indicates the depth of $6.5d_s$, where d_s is the Stokes drift decay length scale, and the dashed black line denotes the depth of $0.4H_B$. The solid magenta and black lines denote H_M and H_B , respectively.

subgridscale terms (Kukulka et al. 2010; Skylingstad et al. 2000).

At location A with LT, the Stokes drift shear production is dominant down to H_{LT} (Fig. 10, top left). The Eulerian shear production first decreases with depth, reaching its minimum value at $z = -0.1H_B$, and then increases with depth and becomes a dominant term at the OSBL base. Augmented P_E at the OSBL base is accompanied by greater buoyancy fluxes, consistent with the local peak of horizontal velocity variance (Fig. 8, top left). In contrast, P_E for the ST case monotonically decays with depth (top right profile in Fig. 10), which is consistent with the relatively weak buoyancy fluxes and the decaying velocity variance profiles at greater depth ($z > 0.6H_B$) (top right profile, Fig. 8). In the absence of LT, neither the pronounced downward TKE fluxes in the surface layer nor the local peak of Eulerian shear production near the mixed layer base is present, even during the rapid mixed layer deepening period. Thus, the TKE budgets at location A reveal that LT induces a greater Eulerian shear production within the shear layer by locally enhanced shear instabilities, which overall drives greater buoyancy fluxes, enhancing the buoyancy entrainment.

4) SCALING OF LT IN MISALIGNED WIND AND WAVE CONDITIONS

The projected surface layer Langmuir number $La_{SL\theta}$ is effective in scaling normalized depth-integrated buoyancy fluxes (see above) and depth-averaged vertical velocity variance under TC conditions with misaligned winds and waves (Rabe et al. 2015; Reichl et al. 2016b). Let us next explore why the scaling with $La_{SL\theta}$ is consistent with a scaling of the dominant TKE budget terms between P_S and $\langle \varepsilon \rangle$ (Fig. 10). Following Kukulka and Harcourt (2017), an LT velocity scale w_L for an idealized TKE balance between P_S and $\langle \varepsilon \rangle$ can be expressed as

$$w_L^3 = H_B^{-1} \int_{-H_B}^0 l(z) P_S(z) dz, \quad (11)$$

where $l(z)$ is a depth-dependent turbulent mixing length. Note that for aligned wind and waves, and for $l = H_B$ (nonlocal mixing), the rhs of Eq. (11) is approximately $u_*^3 La_t^{-2}$, consistent with the scaling proposed by Grant and Belcher (2009). Based on Eq. (11), Kukulka and Harcourt (2017) introduced a modified Langmuir number La_ϕ as

$$La_\phi^{-2} = w_L^3 u_*^{-3} = u_*^{-3} H_B^{-1} \int_{-H_B}^0 l(z) P_S(z) dz. \quad (12)$$

For scaling purposes, let us next assume that the turbulent stress is along the wind direction θ_w , so that Eq. (12) becomes after integration by parts

$$La_\phi^{-2} = \left[\frac{l |\mathbf{u}_s| \cos(\gamma_s - \theta_w)}{H_B u_*} \right]_{-H_B}^0 - \int_{-H_B}^0 \frac{\partial l}{\partial z} \frac{|\mathbf{u}_s| \cos(\gamma_s - \theta_w)}{H_B u_*} dz, \quad (13)$$

where γ_s is the depth-dependent angle of the Stokes drift vector direction. Since l is roughly proportional to z close to the surface and the Stokes drift shear production is predominantly important in the upper 20% of the OSBL (Fig. 10, left; Kukulka and Harcourt 2017), we can further approximate La_ϕ as (see appendix)

$$La_\phi \sim \sqrt{\frac{u_*}{\left| \frac{\cos(\theta_s - \theta_w)}{0.2H_B} \int_{-0.2H_B}^0 \mathbf{u}_s dz \right|}}. \quad (14)$$

Thus, La_ϕ is proportional to $La_{SL\theta}$ in Reichl et al. (2016b) if the Lagrangian shear is aligned with the wind

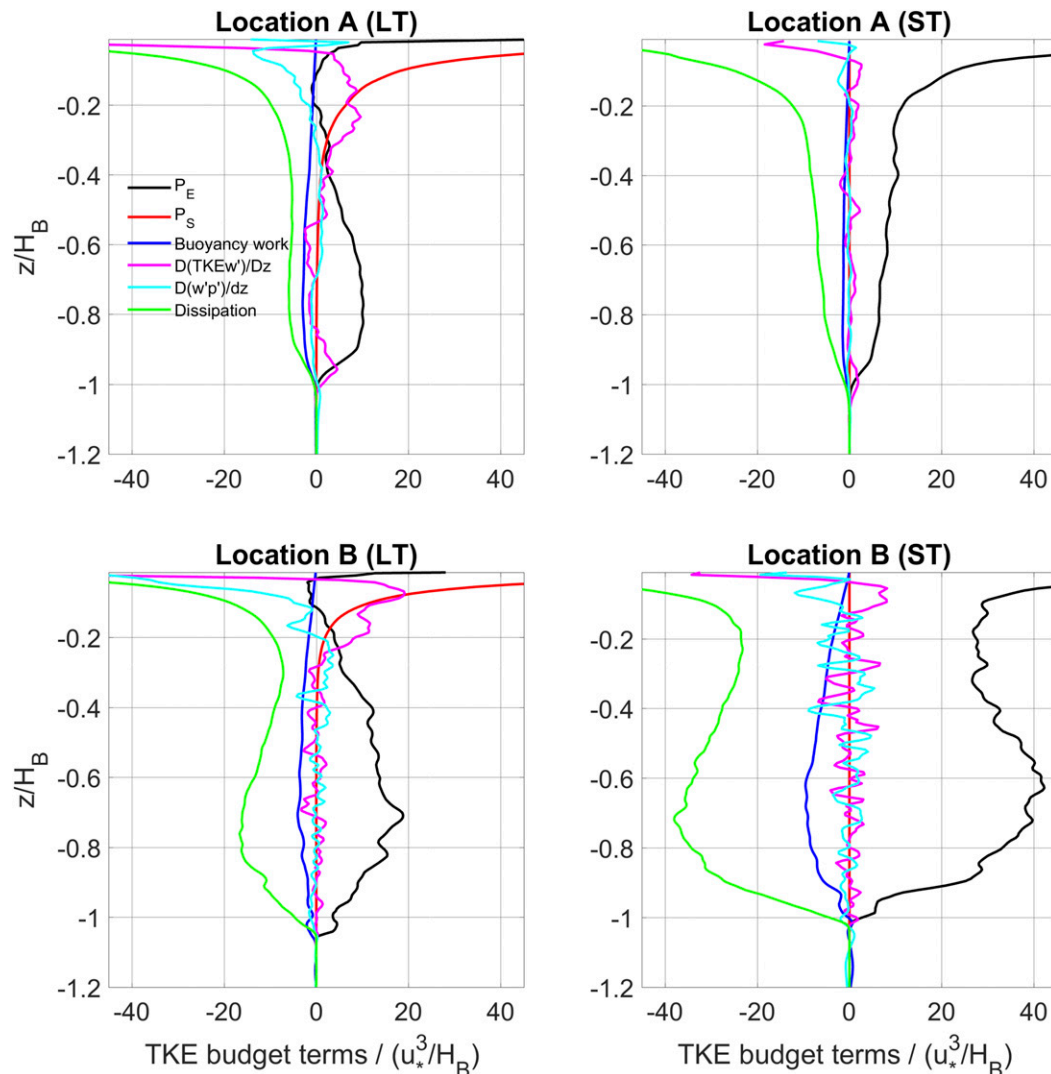


FIG. 10. The normalized TKE budgets at (top) location A and (bottom) location B for (left) the LT case and (right) the ST case: Eulerian shear production (solid black), Stokes drift shear production (solid red), buoyancy work (solid blue), divergence of TKE fluxes (solid magenta), divergence of pressure work (solid cyan), and dissipation rates (solid green).

direction ($\alpha = \theta_w$), which is approximately the case for strong LT if the Eulerian current is well mixed (Fig. 1, bottom right). Thus, the successful scaling of VVV and buoyancy fluxes with $La_{SL\theta}$ can be linked to a leading-order TKE budget analysis.

c. Enhanced entrainment due to energetic inertial currents

To understand the influence of inertial currents on turbulence dynamics, we examine flow properties at location B that is 2.5 RMW behind the TC eye where the ST case shows more energetic buoyancy fluxes and greater mixed layer deepening (Fig. 5, right).

1) CURRENT AND TEMPERATURE PROFILES

Unlike at location A, the magnitude of $\langle u \rangle_{\perp}$ is comparable to $\langle u \rangle_{\parallel}$ and current shear extends below H_E , suggesting the presence of energetic inertial currents that drive turbulence at greater depth (Fig. 7, bottom left). As expected for LT, Eulerian currents are nearly uniform and only weakly sheared in the near-surface layer ($-z < 6.5d_s \approx 0.2H_B$) that is directly influenced by LT (Fig. 7, bottom left; cf. top panel of Fig. 9). However, the LT-affected surface layer at location B is much shallower than at location A, which does not directly influence the deeper shear-driven layer.

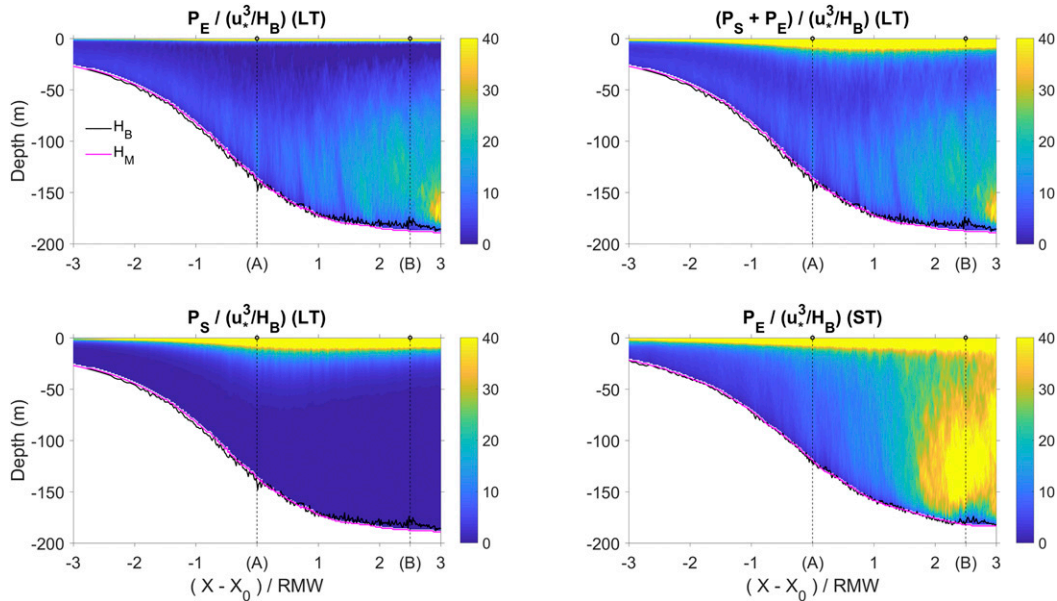


FIG. 11. LES transects of (top left) normalized Eulerian shear production, (bottom left) Stokes drift shear production, (top right) the sum of the normalized Eulerian shear and Stokes drift shear production for the LT case, and (bottom right) the normalized Eulerian shear production for the ST case. Other line styles are as in Fig. 3.

At location B, the temperature differences between the ST and LT cases are smaller compared to location A (Fig. 7, middle) so that buoyancy fluxes for the ST case exceed those of the LT case in regions behind the TC eye (Fig. 5, right). Consistently, Ri profiles are similar for both cases in the shear layer with $Ri < 0.25$ (Fig. 7, bottom right), suggesting that, unlike location A, LT does not influence the deeper layer through locally enhanced shear instabilities.

2) VELOCITY VARIANCE

At location B with LT, the profiles of $\langle u_i^2 \rangle$ near the LT-influenced surface layer ($-z < H_{LT} = 6.5d_s \approx 0.2H_B$) are similar to those at location A for $-z < H_{LT}$ (Fig. 8, bottom left). At greater depth ($-z > H_{LT}$), the horizontal velocity variances exceed $\langle w^2 \rangle$ and the along-wind velocity variance (approximately $\langle v^2 \rangle$) is largest, which is expected for shear-driven turbulence. However, all velocity variances gradually decrease with depth without peak at location B. This is different from location A with LT where LT locally enhances the shear instability near the mixed layer base, resulting in locally enhanced along-wind velocity variances. In the shear layer, velocity variances are significantly larger for the ST than for the LT case, suggesting relatively strong shear turbulence and Eulerian shear production that contributes to the greater entrainment in the ST case.

3) TKE BUDGETS

As for location A, the leading-order budget terms at location B are TKE production and dissipation (Fig. 10, bottom). Unlike location A, the normalized TKE production is now substantially enhanced for the ST case at greater depth, so that the relative magnitude of TKE production terms evolve over time (Fig. 11, bottom right). Near the surface, TKE production remains relatively large because of strong Lagrangian near-surface shear for both ST and LT cases. In the LT case, the total TKE production ($P_S + P_E$) becomes smaller than P_E for the ST case for $(X - X_0)/RMW > 1$ (Fig. 11, right). Since current shear is similar for both LT and ST cases (Fig. 7, bottom left), it is the relatively large turbulent stress in the shear layer ($z < -0.6H_M$) that causes this enhanced P_E in the ST case (Fig. 3, top right).

LT plays two important roles in reducing TKE production at location B. First, Eulerian currents are uniform within $z > -H_{LT} = -0.2H_B$, which reduces P_E (Fig. 10, bottom left). Because the Stokes drift decays over depth H_{LT} , this results in a region near $z = -0.2H_B$ with relatively low TKE production and an associated decrease in TKE and turbulent stresses. Because turbulent stresses are relatively low below H_{LT} , P_E is also substantially smaller in the shear layer, although the current shear is similar for the ST and LT case.

Second, enhanced turbulent near-surface mixing reduces the surface currents and, thus, the surface flux of kinetic energy into the OSBL, which is discussed in the following section.

4) TOTAL ENERGY BUDGETS AND INERTIAL RESONANCE

To understand the relation between turbulence generation and the evolution of inertial currents, we investigate the depth-integrated total energy budget at $(Y - Y_0)/RMW = 1$, based on the governing LES equations:

$$\begin{aligned} \frac{d}{dt} \int_{-H}^0 \left(\frac{1}{2} \langle u_i \rangle \langle u_i \rangle + \frac{1}{2} \langle u'_i u'_i \rangle + \frac{\langle \rho \rangle}{\rho_0} g z \right) dz \\ + \int_{-H}^0 \varepsilon_{ikm} f_k u_{s,m} \langle u_i \rangle dz = \frac{\boldsymbol{\tau}_i \langle \mathbf{u}_i \rangle_0}{\rho_0} + \int_{-H}^0 \langle w' u'_i \rangle \frac{\partial u_{s,i}}{\partial z} dz \\ + \int_{-H}^0 \langle \varepsilon \rangle dz, \end{aligned} \quad (15)$$

where ε_{ikm} is the Levi-Civita tensor and $(f_1, f_2, f_3) = (0, 0, f)$ is the Coriolis vector. The $\boldsymbol{\tau}_i$ and $\langle \mathbf{u}_i \rangle_0$ denote the wind stress vector and surface current vector, respectively. Note that we are considering the depth-integrated energy budget below the wave-breaking layer and assume that breaking energy input is all dissipated locally, consistent with previous LES models under TC (Sullivan et al. 2012; Rabe et al. 2015; Reichl et al. 2016b). The surface flux to mean energy F_{ME} [first term on the rhs of Eq. (15)], the depth-integrated Stokes drift shear production I_{Stokes} [second term on the rhs of Eq. (15)], and depth-integrated dissipation rate D [third term on the rhs of Eq. (15)] are source and sink terms that drive the temporal change of the depth-integrated energy of the system, which partitions into mean kinetic energy (MKE) [first term on the lhs of Eq. (15)], TKE [second term on the lhs of Eq. (15)], and potential energy (PE) [third term on the lhs of Eq. (15)]. The last lhs term of Eq. (15) T_{CS} transfers energy between waves and Eulerian currents due to the Coriolis–Stokes force. This term is much smaller than other budget terms and, therefore, neglected in the following presentation. With these symbols, Eq. (15) is written as

$$F_{ME} + I_{Stokes} + D - \frac{d(MKE)}{dt} - \frac{d(TKE)}{dt} - \frac{d(PE)}{dt} = 0. \quad (16)$$

Throughout the passage of the storm, F_{ME} (black dashed line in Fig. 12a) and, with LT, I_{Stokes} (solid cyan line in Fig. 12a) are predominantly balanced by D (solid

and dashed green lines in Fig. 12a) and changes in mean kinetic energy (solid and dashed red lines in Fig. 12a), which are similar in magnitude. The changes in turbulent kinetic energy (solid and dashed blue lines in Fig. 12a) are small compared to other budget terms. Normalized F_{ME} steadily increases as $\langle \mathbf{u}_i \rangle_0$ increases owing to strong inertial currents. Because inertial currents dissipate relatively slowly, F_{ME} remains relatively large even after the storm passes. With LT, I_{Stokes} is comparable to F_{ME} for $(X - X_0)/RMW < 0.5$, but I_{Stokes} is much smaller than F_{ME} behind the eye for $(X - X_0)/RMW > 1$, when energetic waves propagate away from the storm but inertial currents are still strong.

With LT, the total energy budget dynamics changes at about $(X - X_0)/RMW = 0.5$, when the LT dynamics change from the rapid mixed layer deepening regime to the regime for which LT is relatively shallow and the LT-driven surface layer is decoupled from the deeper shear layer [refer to section 3c(1) and top panel of Fig. 9]. For $(X - X_0)/RMW < 0.5$, that is, during rapid mixed layer deepening, energy is more efficiently used to entrain deeper cool water and to change the potential energy of the system more quickly compared to the ST case (solid magenta line in Fig. 12b). Furthermore, less energy is transferred to inertial currents because in the LT case currents are more mixed vertically and greater vertical shear in the ST case results in relatively large MKE and $d(MKE)/dt$ (red line in Fig. 12b).

For $(X - X_0)/RMW > 0.5$, on the other hand, the relatively shallow LT-influenced near-surface layer causes currents to be more sheared at greater depth inducing a relatively large transfer to MKE, so that MKE changes more in the LT case than the ST case during this period (solid red line in Fig. 12b). Nevertheless, LT mixes near-surface currents so that $\langle \mathbf{u}_i \rangle_0$ is still relatively small, which is accompanied by relatively small F_{ME} compared to the ST case (solid and dashed black lines in Fig. 12a). Thus, the presence of LT weakens the generation of turbulence at greater depth in the shear layer, so that the entrainment and the associated change in potential energy is greater for the ST case once the winds subside (solid magenta line in Fig. 12b).

4. Conclusions

Based on the analysis of high-resolution large-eddy simulation (LES) results, we have investigated the response of the ocean surface boundary layer (OSBL) with and without Langmuir turbulence (LT) to complex wind and wave forcing in tropical cyclone (TC) conditions. The Stokes drift vector that drives LT through the

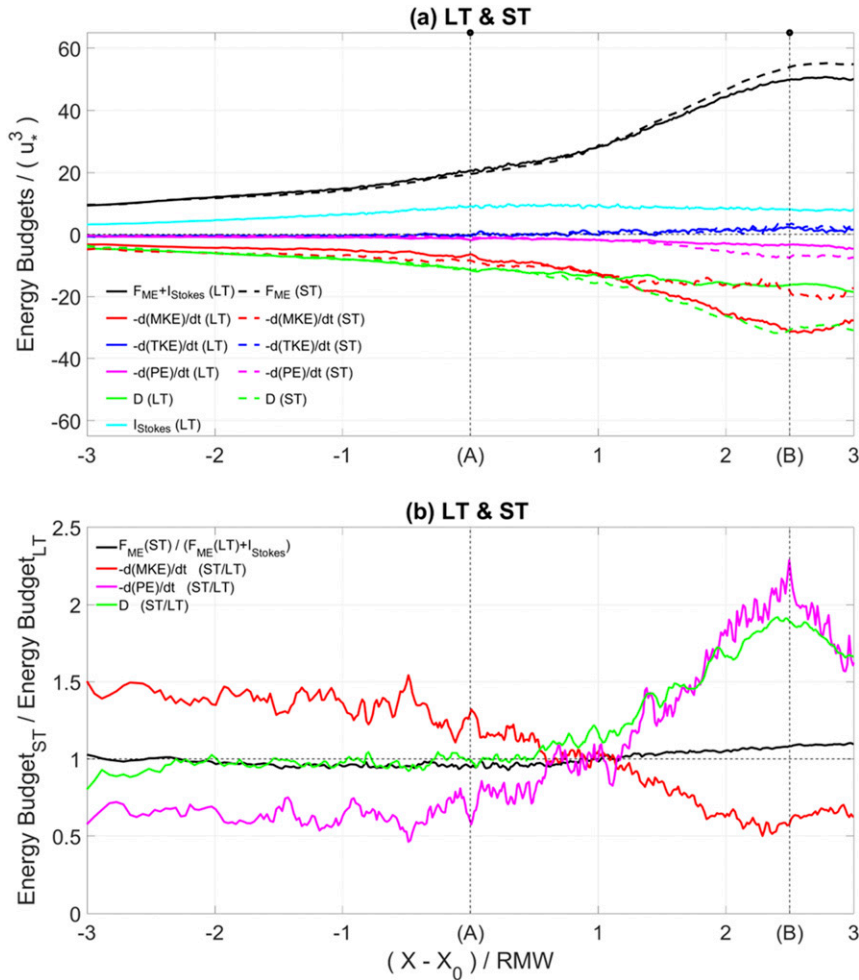


FIG. 12. (a) The LES transect of normalized total energy budgets by u_*^3 in the LT (solid lines) and ST cases (dashed lines) at $(Y - Y_0)/RMW = 1$: the sum of surface flux to mean energy and depth-integrated Stokes drift shear production in the LT case (solid black), depth-integrated Stokes drift shear production only (solid cyan), surface flux to mean currents in the ST case (dashed black), temporal change rates of MKE (solid and dashed red), TKE (solid and dashed blue), PE (solid and dashed magenta), and depth-integrated dissipation rates (solid and dashed green). (b) The total energy budgets in the ST case that are normalized by corresponding terms in the LT case on the same transect: normalized surface flux to mean energy by the sum of surface flux to mean energy in the LT case and depth-integrated Stokes drift shear production (solid black line), normalized temporal change rate of MKE (solid red), PE (solid magenta), and the normalized depth-integrated dissipation rates (solid green).

Craik–Leibovich vortex force is determined from spectral wave simulations obtained from the WAVEWATCH III model. Both the LES and the wave models are forced by winds from the TC Holland wind model. LES experiments are performed with and without LT (i.e., without Stokes drift) and for multiple, densely spaced stations across the TC translation direction, covering the full spatial extent of the TC.

The examination of OSBL depth and entrainment illustrates that LT substantially enhances entrainment with greater buoyancy fluxes, inducing rapid OSBL

deepening during maximum TC winds. The mechanism that drives rapid OSBL deepening is that LT facilitates the downward momentum transport, locally enhancing shear instabilities near the mixed layer base, which occurs only when OSBL depth H_B is relatively shallow compared to a Stokes drift decay length scale d_s . LT enhances vertical velocity variances near a surface layer whose depth H_{LT} is estimated from the enhanced anisotropy of velocity variances. During the rapid OSBL deepening, the LT-affected surface layer is tightly coupled with the deeper shear-driven layer so that H_{LT} is

proportional to H_B . As a result, depth-integrated entrainment fluxes approximately scale with the projected surface layer Langmuir number $La_{SL\theta}$, which is consistent with an idealized TKE budget analysis for misaligned wind and waves.

After the TC passes, H_{LT} is proportional to d_s and the LT-affected surface layer influences relatively weakly the deeper shear-driven layer. In the LT case, the OSBL is characterized by relatively small Lagrangian shear at middepth. At the same time, the normalized surface energy flux to mean currents increases substantially behind the TC eye, exceeding the energy input by the depth-integrated Stokes drift shear production. This is because of strong inertial currents that have been excited by TC winds. LT still homogenizes Eulerian currents in the LT-affected surface layer so that surface currents are reduced in the LT case. The reduced surface currents in the LT case, in turn, reduce the surface energy flux to mean currents, resulting in a smaller total energy input than for the ST case. Here we assume the wind stress and related surface energy fluxes are transferred through the wave breaking layer within which most of the energy input due to breaking waves is all dissipated locally. Together, the small Lagrangian shear at middepth and the reduced total energy input contribute to relatively small TKE levels and entrainment rates for the LT case behind the TC's passage. Therefore, our study illustrates that background currents need to be taken into account for a

complete scaling of LT and its effects on the OSBL under TC conditions.

Acknowledgments. We acknowledge the support of NSF Grants OCE-1130678, OCE-1634578, and OCE-1352422 for funding this work. We also thank the high-performance computing resources as well as information technologies support from NCAR large computation allocation grant, sponsored by National Science Foundation and University of Delaware's high-performance computers Mills and Farber. Two anonymous reviewers provided helpful suggestions that have substantially improved the manuscript.

APPENDIX

Comparison of La_ϕ and $La_{SL\theta}$

To understand the close relation between $La_{SL\theta}$ and La_ϕ , we introduce a unit vector in the wind direction θ_w that is denoted as $\mathbf{N} = \cos(\theta_w)\mathbf{i} + \sin(\theta_w)\mathbf{j}$, where \mathbf{i} and \mathbf{j} are unit vectors in the x and y directions, respectively. Likewise, the Stokes drift vector can be written as $\mathbf{u}_s = |\mathbf{u}_s| \cos(\gamma_s)\mathbf{i} + |\mathbf{u}_s| \sin(\gamma_s)\mathbf{j}$, where γ_s is the direction of Stokes drift. We define θ_s as the direction of $(1/0.2H_B) \int_{-0.2H_B}^0 \mathbf{u}_s dz$, which is the direction of depth-averaged Stokes drift within $0.2H_B$ in Eq. (4). Therefore, the cosine of the misaligned angle between depth-averaged Stokes drift and the wind is

$$\begin{aligned} \cos(\theta_s - \theta_w) &= \frac{\frac{1}{0.2H_B} \int_{-0.2H_B}^0 \mathbf{u}_s dz \cdot \mathbf{N}}{\left| \frac{1}{0.2H_B} \int_{-0.2H_B}^0 \mathbf{u}_s dz \right| |\mathbf{N}|} = \frac{\int_{-0.2H_B}^0 [|\mathbf{u}_s| \cos(\gamma_s)\mathbf{i} + |\mathbf{u}_s| \sin(\gamma_s)\mathbf{j}] \cdot [\cos(\theta_w)\mathbf{i} + \sin(\theta_w)\mathbf{j}] dz}{\left| \int_{-0.2H_B}^0 \mathbf{u}_s dz \right|} \\ &= \frac{\int_{-0.2H_B}^0 |\mathbf{u}_s| [\cos(\gamma_s)\cos(\theta_w) + \sin(\gamma_s)\sin(\theta_w)] dz}{\left| \int_{-0.2H_B}^0 \mathbf{u}_s dz \right|} = \frac{\int_{-0.2H_B}^0 |\mathbf{u}_s| \cos(\gamma_s - \theta_w) dz}{\left| \int_{-0.2H_B}^0 \mathbf{u}_s dz \right|}. \end{aligned} \quad (\text{A1})$$

If we assume the wind direction θ_w is aligned with the direction of depth-averaged Lagrangian shear α and replace $\cos(\theta_s - \alpha)$ in Eq. (4) with $\int_{-0.2H_B}^0 |\mathbf{u}_s| \cos(\gamma_s - \theta_w) dz / \left| \int_{-0.2H_B}^0 \mathbf{u}_s dz \right|$ based on Eq. (A1), $La_{SL\theta}$ becomes

$$La_{SL\theta} = \sqrt{\frac{u_*}{\left| \frac{1}{0.2H_B} \int_{-0.2H_B}^0 |\mathbf{u}_s| \cos(\gamma_s - \theta_w) dz \right|}}, \quad (\text{A2})$$

so that

$$La_{SL\theta}^{-2} \sim \frac{\int_{-0.2H_B}^0 |\mathbf{u}_s| \cos(\gamma_s - \theta_w) dz}{0.2H_B u_*}. \quad (\text{A3})$$

With the assumption that the predominant Stokes drift shear production is only important in the upper 20% of OSBL and l is proportional to z , La_ϕ^2 in Eq. (13) becomes

$$\begin{aligned} \text{La}_\phi^{-2} &\sim \int_{-0.2H_B}^0 \frac{|\mathbf{u}_s| \cos(\gamma_s - \theta_w)}{0.2H_B u_*} dz \\ &= \frac{\int_{-0.2H_B}^0 |\mathbf{u}_s| \cos(\gamma_s - \theta_w) dz}{0.2H_B u_*}. \end{aligned} \quad (\text{A4})$$

By comparing Eq. (A4) to Eq. (A3), we show that $\text{La}_{\text{SL}\theta}$ is proportional to La_ϕ .

REFERENCES

- Belcher, S. E., and Coauthors, 2012: A global perspective on Langmuir turbulence in the ocean surface boundary layer. *Geophys. Res. Lett.*, **39**, L18605, <https://doi.org/10.1029/2012GL052932>.
- Bender, M. A., and I. Ginis, 2000: Real-case simulations of hurricane ocean interaction using a high-resolution coupled model: Effects on hurricane intensity. *Mon. Wea. Rev.*, **128**, 917–946, [https://doi.org/10.1175/1520-0493\(2000\)128<0917:RCOHO>2.0.CO;2](https://doi.org/10.1175/1520-0493(2000)128<0917:RCOHO>2.0.CO;2).
- Blair, A., I. Ginis, T. Hara, and E. Ulhorn, 2017: Impact of Langmuir turbulence on upper ocean response to Hurricane Edouard: Model and observations. *J. Geophys. Res. Oceans*, **122**, 9712–9724, <https://doi.org/10.1002/2017JC012956>.
- Craik, A. D. D., and S. Leibovich, 1976: A rational model for Langmuir circulations. *J. Fluid Mech.*, **73**, 401–426, <https://doi.org/10.1017/S0022112076001420>.
- D’Asaro, E. A., 2014: Turbulence in the upper-ocean mixed layer. *Annu. Rev. Mar. Sci.*, **6**, 101–115, <https://doi.org/10.1146/annurev-marine-010213-135138>.
- , J. Thomson, A. Y. Shcherbina, R. R. Harcourt, M. F. Cronin, M. A. Hemer, and B. Fox-Kemper, 2014: Quantifying upper ocean turbulence driven by surface waves. *Geophys. Res. Lett.*, **41**, 102–107, <https://doi.org/10.1002/2013GL058193>.
- Emanuel, K. A., 1991: The theory of hurricanes. *Annu. Rev. Fluid Mech.*, **23**, 179–196, <https://doi.org/10.1146/annurev.fl.23.010191.001143>.
- , 1999: Thermodynamic control of hurricane intensity. *Nature*, **401**, 665–669, <https://doi.org/10.1038/44326>.
- Fan, Y., I. Ginis, T. Hara, C. W. Wright, and E. J. Walsh, 2009: Numerical simulations and observations of surface wave fields under an extreme tropical cyclone. *J. Phys. Oceanogr.*, **39**, 2097–2116, <https://doi.org/10.1175/2009JPO4224.1>.
- Farmer, D., and M. Li, 1995: Patterns of bubble clouds organized by Langmuir circulation. *J. Phys. Oceanogr.*, **25**, 1426–1440, [https://doi.org/10.1175/1520-0485\(1995\)025<1426:POBCOB>2.0.CO;2](https://doi.org/10.1175/1520-0485(1995)025<1426:POBCOB>2.0.CO;2).
- Gargett, A., and C. E. Grosch, 2014: Turbulence process domination under the combined forcings of wind stress, the Langmuir vortex force, and surface cooling. *J. Phys. Oceanogr.*, **44**, 44–67, <https://doi.org/10.1175/JPO-D-13-021.1>.
- , J. Wells, A. E. Tejada-Martínez, and C. E. Grosch, 2004: Langmuir supercells: A mechanism for sediment resuspension and transport in shallow seas. *Science*, **306**, 1925–1928, <https://doi.org/10.1126/science.1100849>.
- Ginis, I., 2002: Tropical cyclone-ocean interactions. *Atmosphere-Ocean Interactions*, Vol. 1, W. Perrie, Ed., WIT Press, 83–114.
- Grant, A. L. M., and S. E. Belcher, 2009: Characteristics of Langmuir turbulence in the ocean mixed layer. *J. Phys. Oceanogr.*, **39**, 1871–1887, <https://doi.org/10.1175/2009JPO4119.1>.
- , and —, 2011: Wind-driven mixing below the oceanic mixed layer. *J. Phys. Oceanogr.*, **41**, 1556–1575, <https://doi.org/10.1175/JPO-D-10-05020.1>.
- Harcourt, R. R., and E. A. D’Asaro, 2008: Large-eddy simulation of Langmuir turbulence in pure wind seas. *J. Phys. Oceanogr.*, **38**, 1542–1562, <https://doi.org/10.1175/2007JPO3842.1>.
- Holland, G., 1980: An analytic model of the wind and pressure profiles in hurricanes. *Mon. Wea. Rev.*, **108**, 1212–1218, [https://doi.org/10.1175/1520-0493\(1980\)108<1212:AAMOTW>2.0.CO;2](https://doi.org/10.1175/1520-0493(1980)108<1212:AAMOTW>2.0.CO;2).
- , 2008: A revised hurricane pressure–wind model. *Mon. Wea. Rev.*, **136**, 3432–3445, <https://doi.org/10.1175/2008MWR2395.1>.
- Holthuijsen, L. H., M. D. Powell, and J. D. Pietrzak, 2012: Wind and waves in extreme hurricanes. *J. Geophys. Res.*, **117**, C09003, <https://doi.org/10.1029/2012JC007983>.
- Hsu, J.-Y., R.-C. Lien, E. A. D’Asaro, and T. B. Sanford, 2017: Estimates of surface wind stress and drag coefficients in Typhoon Megi. *J. Phys. Oceanogr.*, **47**, 545–565, <https://doi.org/10.1175/JPO-D-16-0069.1>.
- , —, —, and —, 2018: Estimates of surface waves using subsurface EM-APEX floats under Typhoon Fanapi 2010. *J. Atmos. Oceanic Technol.*, **35**, 1053–1075, <https://doi.org/10.1175/JTECH-D-17-0121.1>.
- Kenyon, K. E., 1969: Stokes drift for random gravity waves. *J. Geophys. Res.*, **74**, 6991–6994, <https://doi.org/10.1029/JC074i028p06991>.
- Kukulka, T., and R. R. Harcourt, 2017: Influence of Stokes drift decay scale on Langmuir turbulence. *J. Phys. Oceanogr.*, **47**, 1637–1656, <https://doi.org/10.1175/JPO-D-16-0244.1>.
- , A. J. Plueddemann, J. H. Trowbridge, and P. P. Sullivan, 2009: Significance of Langmuir circulation in upper ocean mixing: Comparison of observations and simulations. *Geophys. Res. Lett.*, **36**, L10603, <https://doi.org/10.1029/2009GL037620>.
- , —, —, and —, 2010: Rapid mixed layer deepening by the combination of Langmuir and shear instabilities: A case study. *J. Phys. Oceanogr.*, **40**, 2381–2400, <https://doi.org/10.1175/2010JPO4403.1>.
- , —, and P. P. Sullivan, 2013: Inhibited upper ocean re-stratification in nonequilibrium swell conditions. *Geophys. Res. Lett.*, **40**, 3672–3676, <https://doi.org/10.1002/grl.50708>.
- Langmuir, I., 1938: Surface motion of water induced by wind. *Science*, **87**, 119–123, <https://doi.org/10.1126/science.87.2250.119>.
- Large, W. G., J. C. McWilliams, and S. C. Doney, 1994: Oceanic vertical mixing: A review and a model with a nonlocal boundary layer parameterization. *Rev. Geophys.*, **32**, 363–403, <https://doi.org/10.1029/94RG01872>.
- Li, M., C. Garrett, and E. Skillingstad, 2005: A regime diagram for classifying turbulent large eddies in the upper ocean. *Deep-Sea Res. I*, **52**, 259–278, <https://doi.org/10.1016/j.dsr.2004.09.004>.
- , S. Vagle, and D. M. Farmer, 2009: Large eddy simulations of upper-ocean response to a midlatitude storm and comparison with observations. *J. Phys. Oceanogr.*, **39**, 2295–2309, <https://doi.org/10.1175/2009JPO4165.1>.
- McWilliams, J. C., and P. P. Sullivan, 2000: Vertical mixing by Langmuir circulations. *Spill Sci. Technol. Bull.*, **6**, 225–237, [https://doi.org/10.1016/S1353-2561\(01\)00041-X](https://doi.org/10.1016/S1353-2561(01)00041-X).
- , —, and C.-H. Moeng, 1997: Langmuir turbulence in the ocean. *J. Fluid Mech.*, **334**, 1–30, <https://doi.org/10.1017/S0022112096004375>.
- , E. Huckle, J.-H. Liang, and P. P. Sullivan, 2012: The wavy Ekman layer: Langmuir circulations, breaking waves, and Reynolds stress. *J. Phys. Oceanogr.*, **42**, 1793–1816, <https://doi.org/10.1175/JPO-D-12-07.1>.
- Noh, Y., G. Goh, S. Raasch, and M. Gryscha, 2009: Formation of a diurnal thermocline in the ocean mixed layer simulated by LES. *J. Phys. Oceanogr.*, **39**, 1244–1257, <https://doi.org/10.1175/2008JPO4032.1>.

- Plueddemann, A. J., J. A. Smith, D. M. Farmer, R. A. Weller, W. R. Crawford, R. Pinkel, S. Vagle, and A. Gnanadesikan, 1996: Structure and variability of Langmuir circulation during the Surface Waves Processes Program. *J. Geophys. Res.*, **101**, 3525–3543, <https://doi.org/10.1029/95JC03282>.
- Polton, J. A., and S. E. Belcher, 2007: Langmuir turbulence and deeply penetrating jets in an unstratified mixed layer. *J. Geophys. Res.*, **112**, C09020, <https://doi.org/10.1029/2007JC004205>.
- Price, J. F., 1981: Upper ocean response to a hurricane. *J. Phys. Oceanogr.*, **11**, 153–175, [https://doi.org/10.1175/1520-0485\(1981\)011<0153:UORTAH>2.0.CO;2](https://doi.org/10.1175/1520-0485(1981)011<0153:UORTAH>2.0.CO;2).
- Rabe, T. J., T. Kukulka, I. Ginis, T. Hara, B. G. Reichl, E. A. D'Asaro, R. R. Harcourt, and P. P. Sullivan, 2015: Langmuir turbulence under Hurricane Gustav (2008). *J. Phys. Oceanogr.*, **45**, 657–677, <https://doi.org/10.1175/JPO-D-14-0030.1>.
- Reichl, B. G., I. Ginis, T. Hara, B. Thomas, T. Kukulka, and D. Wang, 2016a: Impact of sea-state-dependent Langmuir turbulence on the ocean response to a tropical cyclone. *Mon. Wea. Rev.*, **144**, 4569–4590, <https://doi.org/10.1175/MWR-D-16-0074.1>.
- , D. Wang, T. Hara, I. Ginis, and T. Kukulka, 2016b: Langmuir turbulence parameterization in tropical cyclone conditions. *J. Phys. Oceanogr.*, **46**, 863–886, <https://doi.org/10.1175/JPO-D-15-0106.1>.
- Sanford, T. B., J. F. Price, and J. B. Girton, 2011: Upper-ocean response to Hurricane Frances (2004) observed by profiling EM-APEX floats. *J. Phys. Oceanogr.*, **41**, 1041–1056, <https://doi.org/10.1175/2010JPO4313.1>.
- Skillingstad, E. D., and D. W. Denbo, 1995: An ocean large-eddy simulation of Langmuir circulations and convection in the surface mixed layer. *J. Geophys. Res.*, **100**, 8501–8522, <https://doi.org/10.1029/94JC03202>.
- , W. D. Smyth, J. N. Moum, and H. W. Wijesekera, 1999: Upper-ocean turbulence during a westerly wind burst: A comparison of large-eddy simulation results and microstructure measurements. *J. Phys. Oceanogr.*, **29**, 5–28, [https://doi.org/10.1175/1520-0485\(1999\)029<0005:UOTDAW>2.0.CO;2](https://doi.org/10.1175/1520-0485(1999)029<0005:UOTDAW>2.0.CO;2).
- , —, and G. B. Crawford, 2000: Resonant wind-driven mixing in the ocean boundary layer. *J. Phys. Oceanogr.*, **30**, 1866–1890, [https://doi.org/10.1175/1520-0485\(2000\)030<1866:RWDMIT>2.0.CO;2](https://doi.org/10.1175/1520-0485(2000)030<1866:RWDMIT>2.0.CO;2).
- Smith, J. A., 1992: Observed growth of Langmuir circulation. *J. Geophys. Res.*, **97**, 5651–5664, <https://doi.org/10.1029/91JC03118>.
- Sullivan, P. P., and J. C. McWilliams, 2010: Dynamics of winds and currents coupled to surface waves. *Annu. Rev. Fluid Mech.*, **42**, 19–42, <https://doi.org/10.1146/annurev-fluid-121108-145541>.
- , L. Romero, J. C. McWilliams, and W. K. Melville, 2012: Transient evolution of Langmuir turbulence in ocean boundary layers driven by hurricane winds and waves. *J. Phys. Oceanogr.*, **42**, 1959–1980, <https://doi.org/10.1175/JPO-D-12-025.1>.
- Thorpe, S., 2004: Langmuir circulation. *Annu. Rev. Fluid Mech.*, **36**, 55–79, <https://doi.org/10.1146/annurev.fluid.36.052203.071431>.
- Tolman, H. L., 2009: User manual and system documentation of WAVEWATCH-IIIITM version 3.14. NOAA/NWS/NCEP Tech. Note, 220 pp., http://polar.ncep.noaa.gov/mmab/papers/tt276/MMAB_276.pdf.
- Van Roekel, L. P., B. Fox-Kemper, P. P. Sullivan, P. E. Hamlington, and S. R. Haney, 2012: The form and orientation of Langmuir cells for misaligned winds and waves. *J. Geophys. Res.*, **117**, C05001, <https://doi.org/10.1029/2011JC007516>.
- Weller, R. A., and J. F. Price, 1988: Langmuir circulations within the oceanic mixed layer. *Deep-Sea Res.*, **35**, 711–747, [https://doi.org/10.1016/0198-0149\(88\)90027-1](https://doi.org/10.1016/0198-0149(88)90027-1).
- Zilitinkevich, S., I. Esau, and A. Baklanov, 2007: Further comments on the equilibrium height of neutral and stable planetary boundary layers. *Quart. J. Roy. Meteor. Soc.*, **133**, 265–271, <https://doi.org/10.1002/qj.27>.